

pubs.acs.org/JPCL Letter

# Distinguishing Energy- and Charge-Transfer Processes in Layered Perovskite Quantum Wells with Two-Dimensional Action Spectroscopies

Ninghao Zhou,<sup>†</sup> Zhenyu Ouyang,<sup>†</sup> Jun Hu, Olivia F. Williams, Liang Yan, Wei You, and Andrew M. Moran\*



Cite This: J. Phys. Chem. Lett. 2020, 11, 4570–4577



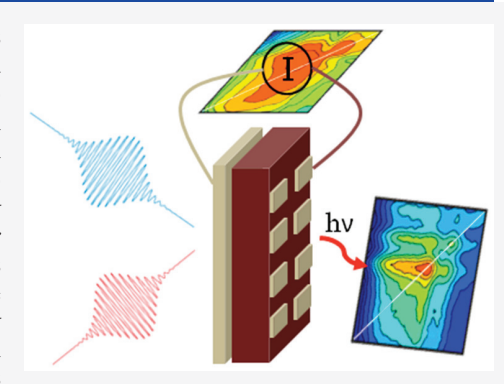
**ACCESS** 

Metrics & More



Supporting Information

ABSTRACT: Interest in photovoltaic devices based on layered perovskites is motivated by their tunable optoelectronic properties and stabilities in humid conditions. In these systems, quantum wells with different sizes are organized to direct energy and charge transport between electrodes; however, these relaxation mechanisms are difficult to distinguish based on conventional transient absorption techniques. Here, two-dimensional "action spectroscopies" are employed to separately target processes that lead to the production of photocurrent and energy loss due to fluorescence emission. These measurements show that energy transfer between quantum wells dominates the subnanosecond time scale, whereas electron transfer occurs at later times. Overall, this study suggests that while the intense exciton transitions promote light harvesting, much of the absorbed energy is lost by way of spontaneous emission. This limitation may be overcome with alternate layered perovskite systems that combine smaller exciton binding energies with large absorbance cross sections in the visible spectral range.



Interest in organohalide perovskites is motivated by their potential for use in optoelectronic devices. Although perovskite solar cells had been considered previously, the development of all-solid-state architectures initiated a rapid increase in the efficiencies of these systems from 11% in 2012<sup>2,3</sup> to more than 25% by 2019. Organohalide perovskites can be processed from solution and have absorbance spectra that are readily tuned with control of the halide ratio and metal cation. Toxicity of Pb and long-term stability are two challenges that still face these materials; however, recent work suggests that quantum-confined two-dimensional (2D) perovskites may be employed to address the problem of long-term stability while maintaining solar cell efficiencies on the order of 18%. P-12

In layered perovskite films, the thinnest and thickest quantum wells are most concentrated at the glass- and air-sides of the films, respectively.  $^{12-14}$  While this layering effect has been established with purely optical techniques,  $^{15-17}$  recent FIB milling experiments show that the distribution of quantum wells changes only slightly with respect to depth in a film.  $^{18}$  Nonetheless, as indicated in Figure 1, the concentration gradients may direct energy and charge transport processes between interfaces due to monotonic changes in the average values of the band gaps and energy levels. For example, the quantum wells investigated in this work are described by the formula  $(BA)_2(MA)_{n-1}[Pb_nI_{3n+1}]$ , where MA is methylammonium and BA is n-butyl ammonium.  $^{13,19}$  The excitons in

quantum wells with n=2, 3, and 4 absorb light near 570, 600, and 640 nm, respectively, thereby promoting a cascade of energy-transfer transitions from the glass- to air-sides of a film. In addition, the staggered valence and conduction bands promote electron and hole transport in the same and opposing directions in systems with type I and II electronic structures, respectively. For example, type I and II band alignments are represented with shaded and open rectangles in Figure 1a. Direct measurements of the energy levels in pure-phase n=1 and bulk systems suggest a type I electronic structure, whereas transient absorption studies have assumed a type II configuration.  $^{15,22}$  In addition, heterogeneity in the band alignment induced by thermal fluctuations has been investigated in a recent theoretical study.  $^{23}$ 

In this work, we use complementary "action spectroscopies" to distinguish energy- and charge-transfer dynamics in layered perovskite systems. First, nonlinear photocurrent spectroscopy (NLPC) is applied to photovoltaic cells based on layered perovskite films. <sup>28</sup> As shown in Figure 1,

 Received:
 March 16, 2020

 Accepted:
 May 19, 2020

 Published:
 May 19, 2020





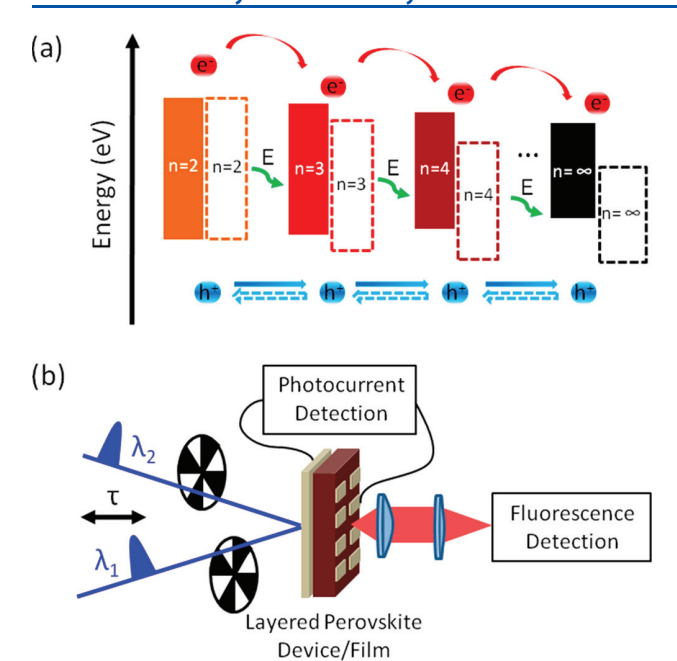


Figure 1. NLPC and NLFL techniques are used to probe charge- and energy-transfer processes in layered perovskite systems. (a) Band gaps of the quantum wells decrease as the index of the quantum well, n, increases. Electron and energy transfer are promoted toward the largest quantum wells. The direction of hole transport is still under investigation because a consensus has not been reached regarding whether the system possesses a type I (shaded rectangles) or type II (open rectangles) band alignment. (b) In NLPC spectroscopy, the nonlinear response of the photocurrent is isolated by chopping two color-tunable laser pulses with an experimentally controlled delay time,  $\tau$ . NLFL spectroscopy is conducted with a similar experimental setup; however, fluorescence emission is detected in the 700–750 nm range.

the nonlinear response of a device to a pair of color-tunable laser pulses is measured as a function of the delay between pulses. The present study differs from our recent application of the NLPC method to a separate layered perovskite system<sup>32</sup> in that the current films possess larger quantum wells with smaller binding energies, thereby making charge-transfer pathways more apparent. Second, nonlinear fluorescence (NLFL) spectroscopy is used to selectively probe energy-transfer mechanisms. The NLFL technique is conducted using essentially the same procedure as that employed for a NLPC experiment; however, fluorescence emission is collected in the 700-750 nm range rather than processing the photocurrent. Assuming that radiative recombination is a primary mechanism for energy loss in a photovoltaic device, NLFL and NLPC spectroscopies account for the majority of processes initiated by light absorption. To this end, it is worth noting that the NLFL and NLPC techniques can be compared on the same footing from the perspective of time-dependent perturbation theory, whereas transient absorption spectroscopy is described by a lower-order response function. Nonetheless, it is useful to consider that these action spectroscopies possess terms analogous to ground-state bleach, excited-state emission, and excited-state absorption signal components in transient absorption spectroscopy. <sup>26,29–31</sup>

Two-dimensional NLPC spectra acquired at delay times ranging from 1 to 2000 ps are shown in the top row of Figure 2. The spectra are dominated by broad features that are

superposed with narrow (~20 nm widths) exciton resonances on the diagonal of the spectrum near 570, 600, and 640 nm (n = 2, 3, and 4 quantum wells). The prominence of features with broad line widths is consistent with large contributions from a continuum of excited states. 32,33 As discussed in recent work, 28 this aspect of the NLPC spectra differs significantly from transient absorption signals, which are dominated by excitons and have relatively small contributions from continuum states.  $^{16,17}$  Excitons in the n=4 quantum wells dissociate on the nanosecond time scale as evidenced by the disappearance of the diagonal peak near 640 nm by  $\tau$  = 2000 ps; the decay of this diagonal peak is not assigned to spontaneous emission because the time scale is relatively short and all signal components are weighted by the production of photocurrent in NLPC spectra. In contrast, the broad components of the signal persist for a length of time far longer the delay range accessible with this instrument. Interestingly, signal intensity accumulates in a cross peak near  $\lambda_1 = 570$  nm and  $\lambda_2 = 600$ – 640 nm as the delay time increases. In principle, such redshifting of the signal intensity along the  $\lambda_2$  axis may represent either energy or electron transfer as both processes can lead to the production of photocurrent depending on assumptions made about the relaxation scheme. For example, energytransfer processes initiated in the n = 2 system may first concentrate electronic excitations in the larger quantum wells, where exciton dissociation is more probable.

In order to understand the competing relaxation mechanisms in this system, the NLFL spectra shown in the bottom row of Figure 2 are acquired at the same four delay times employed for the NLPC measurements. To begin, like transient absorption signals, 16,17 it is clear by inspection that the exciton resonances are far more prominent in the NLFL spectra. In earlier work, we have suggested that enhanced contributions of continuum states in linear external quantum efficiency and NLPC signals originate in a greater propensity for charge separation.<sup>28</sup> Intense peaks associated with the n = 3and 4 quantum wells are located on the diagonal of the spectrum near 600 and 640 nm at  $\tau = 1$  ps. The peak associated with the n = 2 quantum well is smaller because of its concentration and lower probability of directly transferring energy to the n > 5 quantum wells from which fluorescence emission is detected (i.e., a significant fraction of excitons in the n = 2 quantum wells relax by way of radiative recombination). 16 The 600 nm diagonal peak persists at all delay times, whereas the relative intensity of the 640 nm diagonal peak decays on the subnanosecond time scale. As this behavior is observed with both the NLFL and NLPC techniques, we hypothesize that the excitons in the n=4quantum wells dissociate more rapidly because the binding energies decrease as the value of n increases.<sup>33</sup> Consistent with this interpretation, marked differences in the free carrier concentrations associated with the n = 3 and 4 quantum wells have been detected using transient absorption microscopy.<sup>18</sup>

NLFL cross peaks between the n = 3 ( $\lambda_1 = 600$  nm) and n = 4 and 5 ( $\lambda_2 = 640$  and 680 nm) quantum wells are detected above the diagonal at  $\tau = 1$  ps delay. Such cross peaks appear on pulse width-limited time scales because the n = 4 and 5 quantum wells directly absorb portions of the 600 nm laser beam via their continua of excited states (i.e., these cross peaks do not necessarily reflect nonradiative transitions induced by light absorption). Compared to the diagonal peak at 600 nm, the relative intensities of the cross peaks above the diagonal grow as the delay time increases as a result of energy transfer

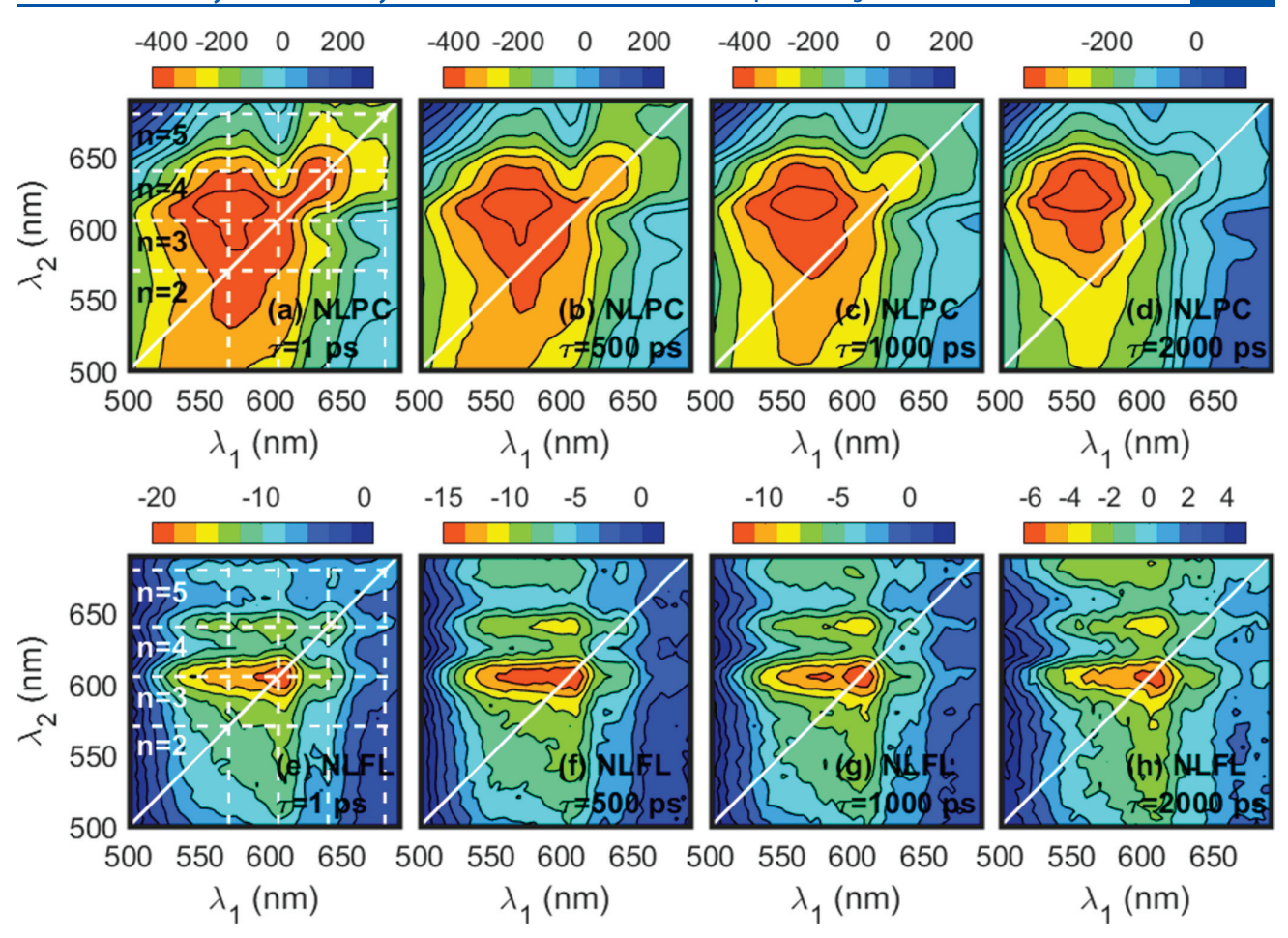


Figure 2. Two-dimensional NLPC (top) and NLFL (bottom) spectra acquired at (a and e) 1 ps, (b and f) 500 ps, (c and g) 1000 ps, and (d and h) 2000 ps. Electron- and energy-transfer processes induce red-shifts along the  $\lambda_2$  axis for the NLPC and NLFL spectra, respectively. For both axes, peaks associated with the n=2, 3, 4, and 5 quantum wells are located at 570, 600, 640, and 680 nm. The NLPC and NLFL signals are reported in units of nA and mV, respectively.

between quantum wells. For example, the relative intensity of the cross peak between the n=3 and 4 quantum wells increases between the 1 and 500 ps delay times as evidenced by the change in contour lines (i.e., green at 1 ps and yellow at 500 ps). The cross peak between the n=3 and 5 quantum wells grows more slowly because the n=5 quantum wells are populated by way of a sequence of energy-transfer transitions (i.e., the n=4 quantum well may be populated as an intermediate in the transfer of energy from the n=3 to n=5 quantum wells).  $^{16,17}$ 

The two sets of action spectra provide complementary insights into photoinduced dynamics. The NLPC signal components are sensitive to charge-transfer processes because they are weighted by the amount of photocurrent produced by the device,  $^{26,34}$  whereas NLFL signal components primarily reflect energy transfer and the radiative recombination of excitons. Further insights into the nature of the dynamics may be gathered by comparing the NLPC and NLFL temporal profiles in Figure 3. These data show that the processes observed with NLPC spectroscopy are slower and exhibit either rising or decaying profiles depending on the particular set of wavelengths,  $\lambda_1$  and  $\lambda_2$ . For example, when  $\lambda_1$  is tuned to 570 or 600 nm, the NLPC signal intensity rises at longer wavelengths,  $\lambda_2$ , on the nanosecond time scale, which signifies electron transfer from smaller to larger quantum wells. In

contrast, the NLPC signals decay monotonically as the delay time increases when the system is excited at  $\lambda_1 = 640$  nm, thereby ruling out type II hole transfer as depicted in Figure 1. That is, if holes transfer from larger to smaller quantum wells, the NLPC signal magnitudes at  $\lambda_2 = 570$  nm should rise when the n = 4 quantum wells are photoexcited at  $\lambda_1 = 640$  nm (see Figure 3c). It was proposed that such rising signal profiles have been detected by transient absorption spectroscopy, although we find no evidence of this in our own transient absorption data (see the Supporting Information). 16,17 Thus, the NLPC temporal profiles suggest that either the system possesses a type I band alignment or the efficiency of type II hole transfer is negligible. In contrast, the NLFL signals decay at all combinations of wavelengths. This aspect of the NLFL response is consistent with transient absorption data acquired for layered perovskite systems which show that energy transfer occurs in parallel with excited-state deactivation at layer edge states, thereby inducing an overall decay in signal intensity.  $^{14,16,17}$ 

As discussed previously,  $^{16,17}$  energy-transfer processes in layered perovskites are promoted by large exciton binding energies (e.g., 150 meV for the n=3 quantum well) $^{33}$  and transition dipoles (>10 D) $^{35}$  as well as the close proximities of the quantum wells ( $\sim$ 1 nm). $^{36}$  In addition, it is instructive to consider that electron transfer is a shorter-range process in

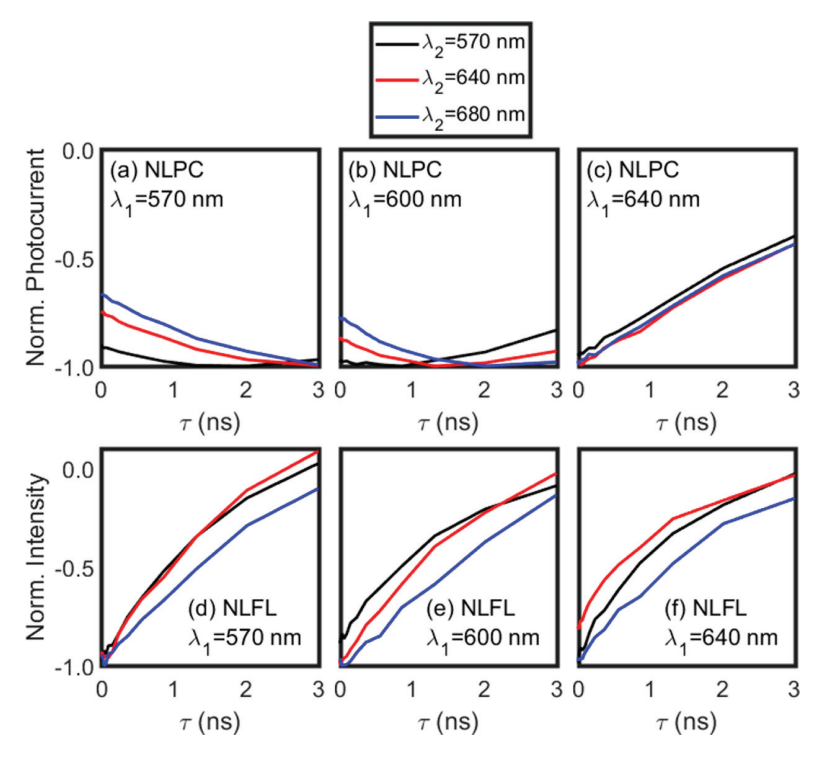


Figure 3. Temporal profiles of NLPC (top) and NLFL (bottom) signals at various wavelengths,  $\lambda_1$  and  $\lambda_2$ . (a–c) The rising NLPC signal strengths displayed in panels a and b suggest that electron-transfer processes are initiated in the n=2 ( $\lambda_1=570$  nm) and 3 ( $\lambda_1=600$  nm) quantum wells, respectively. Type II hole transfer is ruled out based on the monotonic decay of the signal magnitude in panel c. (d–f) The NLFL signals exhibit an overall decay as the delay time increases, which is consistent with transient absorption signals previously reported for layered perovskites. In all panels, the signals are normalized to the points with the largest magnitudes.

which the rate decreases exponentially with the distance between the donor and acceptor,<sup>37</sup> whereas the energy-transfer rate scales as either the inverse fourth or sixth power of the distance between the donor and acceptor depending on the geometry of the system.<sup>38,39</sup> For example, if the transition dipole coupling is taken to scale as the inverse cube of the distance between the donor and acceptor, the Coulombic interaction between the n=2 and 3 quantum wells in layered perovskite can be estimated with 60 meV nm³/d³, where d is the distance between dipoles in nanometers.<sup>16</sup> Thus, transition dipole couplings on the order of tens of meV, which are on par with those involving chromophores in photosynthetic light-harvesting proteins,<sup>40</sup> are anticipated in layered perovskites. These aspects of layered perovskite systems suggest that energy transfer should readily outcompete charge transfer on short time scales.

The signals presented in Figure 3 do not contain evidence of hole transfer from larger to smaller quantum wells as expected for type II electronic structure (see Figure 1). For this reason, it should be considered that evidence of type II electronic structure in layered perovskites is rooted in a controversial interpretation of transient absorption signals.  $^{15-17,22}$  In these experiments, photoexcitation of the n=6 quantum well at 700 nm induces quasi-instantaneous responses in smaller quantum wells at shorter wavelengths. These cross peaks have been assigned to ultrafast hole-transfer processes, although the reported time scales vary by 3 orders of magnitude in recent literature (0.3-987 ps). It is our view that the most likely explanation for these cross peaks has been overlooked despite the large transition dipole couplings between quantum wells.  $^{16,17}$  While it is true that cross peaks may be induced

by nonradiative transitions, it is also well-established that these resonances appear in the ground state bleach nonlinearities of coupled systems. <sup>41,42</sup> These technical aspects of the transient absorption signal generation mechanism are discussed along-side previously acquired experimental data in the Supporting Information.

Our NLPC data indicate that the present system either possesses type I band alignments or that it is type II and the efficiency of hole transfer is negligible. We reach this conclusion based on the information provided by separate experimental techniques. First, as mentioned above, the suggestion that holes transfer from larger to smaller quantum wells is based on a questionable interpretation of cross peaks in transient absorption spectra. Second, the NLPC signals presented in Figures 2 and 3 contain signatures of electron transfer from smaller to larger quantum wells but are devoid of evidence for type II hole-transfer dynamics. NLPC spectroscopy is specially equipped to establish the directions of charge flow in a photovoltaic device because, unlike transient absorption spectroscopy, relaxation processes that ultimately lead to spontaneous emission do not contribute to the nonlinear response.

The relaxation scheme summarized in Figure 4 takes into account earlier transient absorption spectroscopy<sup>16,17</sup> and microscopy<sup>18</sup> data in addition to the present NLPC and NLFL experiments. While it is generally accepted that light absorption by smaller quantum wells initiates parallel energy-and charge-transfer dynamics, a consensus has not been reached regarding the rates and efficiencies of specific relaxation pathways as they are difficult to pinpoint because of the complexity of the system. Our earlier analysis of

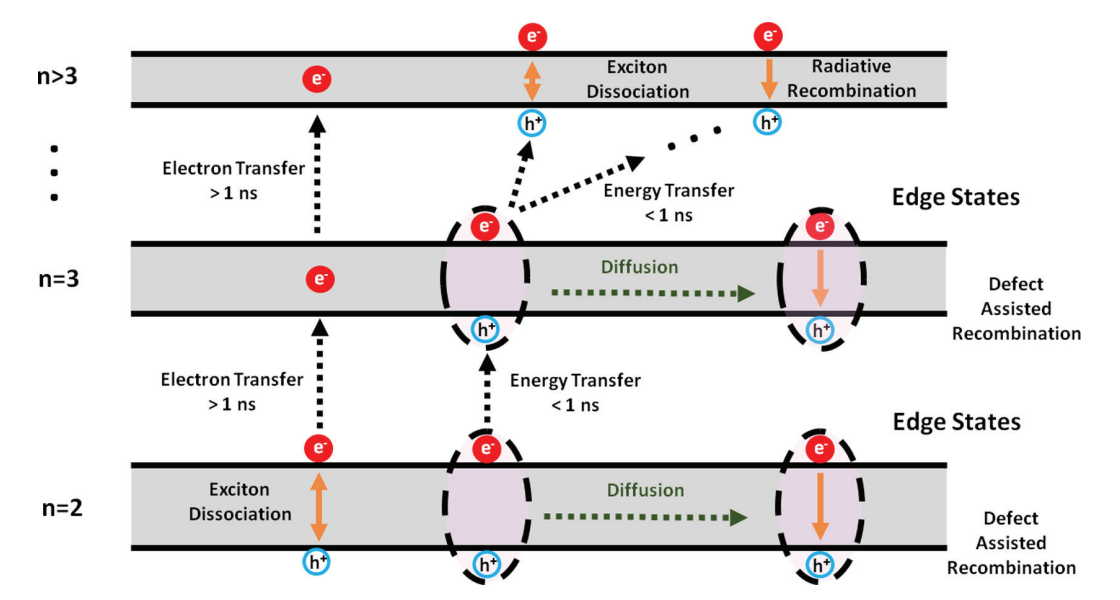


Figure 4. Photoinduced relaxation scheme for layered perovskite quantum wells. Energy and electron transfer proceeds toward the largest quantum wells on time scales shorter and longer than 1 ns, respectively. This scheme suggests that the n = 2 system is initially populated; however, the competition between energy- and electron-transfer processes applies generally to photoexcitation of all quantum wells. The efficiency of exciton dissociation increases with the value of n because of a concomitant decrease in the exciton binding energy.

transient absorption data suggests that roughly 50% of the excitons in the n = 2 quantum well undergo energy-transfer transitions to larger quantum wells. 16,17 The present NLFL spectra confirm the activities of these energy-transfer pathways as the growth of cross peaks involving excitons in the n = 3-5quantum wells is observed on the subnanosecond time scale. In addition, we have estimated that roughly 50% of excitons either recombine at the layer edges or dissociate and undergo subsequent electron-transfer transitions. 16,17 The NLPC technique is far more sensitive to charge-transfer mechanisms than are purely optical spectroscopies because the signal components reflect the action spectrum of the device (i.e., the production of photocurrent). Finally, all experiments conducted to date suggest that the energy-transfer processes occur on a shorter time scale (0.1-1 ns) than do electrontransfer transitions (>1 ns). This separation in time scales is approximate but justified by available experimental data and an analysis of the parameters that govern the rates (e.g., the length scaling of donor-acceptor interactions). 16,17

The present system possesses a large absorption cross section for the same reasons that energy is efficiently transferred between quantum wells (i.e., large transition dipoles and binding energies). Transient absorption microscopies, which are particularly sensitive to exciton dissociation processes, show that free charge carriers become prevalent only in quantum wells with n > 3. This aspect of the system is not ideal because this means that much of the light absorbed at wavelengths shorter than 640 nm results in radiative loss. On the basis of these data, we hypothesize that properties intermediate between those of the present material and a bulk perovskite are more ideally suited for photovoltaic applications.

The limitations of the present system may be minimized with layered perovksites in which the resonances of larger quantum wells with smaller binding energies are located in the visible spectral range. For example, layered 2D perovskites in which iodide is replaced by bromide possess exciton

resonances near 477, 496, and 540 nm for the n=4, 5, and  $\infty$  quantum wells, respectively. Moreover, if these wavelengths are not ideal, the resonances of mixed halide systems can interpolate between those associated with only iodide and bromide. In an alternate approach, 2D and 3D perovskite phases may be mixed to improve the power conversion efficiencies of photovoltaic cells. Py optimizing the ratios of 2D and 3D phases, the layered architecture (i.e., charge and energy funnel) and resistance to moisture are maintained without compromising the photocurrents induced by larger quantum wells and the bulk phase. While the present data suggest that these are promising directions, layered perovskite systems are quite complex, and further investigations of these relaxation mechanisms will be required to optimize solar cells based on these materials.

In summary, the present experiments confirm that a cascade of electron- and energy-transfer processes is initiated by photoexcitation of smaller quantum wells in layered perovskite systems. These relaxation mechanisms are difficult to distinguish with conventional transient absorption techniques but are selectively detected with NLPC and NLFL experiments. These data show that energy transfer occurs on the subnanosecond time scale, whereas electron transfer occurs at later times. In addition, we do not find evidence of type II hole transport as depicted in Figure 1. This conclusion is particularly robust because it is directly reflected in the absence of rising signal magnitudes in Figure 3c; the result does not require a deconvolution of signal components and/or acceptance of a particular version of the response function. Overall, the combination of spectroscopic data that has been acquired for this layered perovksite system confirms that the large exciton binding energies associated with smaller quantum wells favor energy transfer and loss by way of fluorescence emission. This aspect of the system is undesirable for solar cells but may be overcome by modifying the chemical compositions and/or amount of quantum confinement in the material.

# **■** METHODS

Device Fabrication. Precursors for device fabrication were prepared or obtained as follows. Methylammonium iodide (MAI) was synthesized by the reaction of stoichiometric ratio of unstabilized HI solution (57 wt % in water, Sigma-Aldrich, purified by 0.36 M tributyl phosphate solution in chloroform) and methylamine solution (40 wt % in water, Sigma-Aldrich) in an ice bath. The crude MAI was precipitated by adding plenty of ethyl ether and purified by the recrystallization in ethanol. Butylammonium iodide (BAI) was synthesized by the reaction of stoichiometric ratio of unstabilized HI solution (57 wt % in water, Sigma-Aldrich, purified by 0.36 M tributyl phosphate solution in chloroform) and n-butylamine (Sigma-Aldrich) in an ice bath. The crude BAI was obtained by evaporating the solvent under reduced pressure. Pure BAI was produced by recrystallization of the crude product in ethanol.

The device fabrication followed our previous work.<sup>32</sup> In detail, indium-doped tin oxide (ITO) coated glass substrates (20  $\Omega$ /sq sheet resistance, from Thin Film Devices, Inc.) were first cleaned with ultrasonic waves in deionized water, acetone, and 2-proponal for 15 min each. Nitrogen gas was then used to dry substrates followed by a 15 min UV-ozone treatment. After the samples were filtered by a 0.45  $\mu$ m poly(vinylidene difluoride) filter, the PEDOT:PSS water dispersion (Clevios P VP AI 4083 from Heraeus) was spin coated on substrates at 4000 rpm for 60 s to deposit a 40 nm thick hole transport layer. Films were heated at 130 °C in the air for 15 min. The 2D perovskite precursor solutions were made by dissolving BAI, MAI, and PbI<sub>2</sub> (99.9985%, from Alfa Aesar) in dimethylformamide (DMF; from Sigma-Aldrich) with stoichiometric ratios of 2:2:3. The precursor concentration of Pb<sup>2+</sup> was 1 M. Before spin coating, the precursor solution was heated at 70 °C and substrates were heated at 150 °C for 15 min. Then the precursor solution was quickly spun cast on substrates at 5000 rpm for 20 s to form the 2D perovskite layer. After the deposition of the 2D perovskite layer, a [6,6]phenyl C61 butyric acid methyl ester (PCBM) solution in chloroform with a concentration of 13 mg/mL was spin-coated on top at 2000 rpm for 30 s. Films were spin-coated on the PCBM layer with a bathophenanthroline solution in ethanol with a concentration of 0.7 mg mL<sup>-1</sup> at 4000 rpm for 30 s. Finally, 100 nm Cu was deposited on the film as the top contact through thermal evaporation at a base pressure of 2  $\times$  $10^{-6}$  mbar or lower. The active area of the device was 0.13 cm<sup>2</sup>.

Fabrication of thin films was conducted as follows. n-Butylammonium iodide (BAI) was obtained from Sigma; MAI was purchased from Solaronix, and lead iodide (99.999%) was obtained from Alfa-Aesar. All chemicals were used without further purification. Fluorine-doped tin oxide (FTO) substrates (1 in.  $\times$  1 in., 7– $10~\Omega/sq$  sheet resistance from MTI) were cleaned via sonication in a series of four solvents: Contrex AP glassware detergent in deionized water, deionized water, acetone, and isopropanol for 20 min each. Following the isopropanol wash, the substrates were dried in a stream of nitrogen gas.

Cleaned FTO substrates were preheated in air at 100  $^{\circ}$ C for 30 min. A 150  $\mu$ L aliquot of the precursor (0.232 g BAI, 0.184 g MAI, and 0.800 g lead iodide dissolved in 2 mL DMF) was spin coated on the preheated substrates at 3000 rpm (1500 rpm/s acceleration) for 20 s.

NLPC and NLFL Spectroscopy. Action spectroscopies are conducted using the instrument described in previous work.<sup>28</sup>

All experiments are conducted with a 45 fs, 4 mJ Coherent Libra laser system. To begin, 1.5 mJ of the 800 nm fundamental is focused into a 2 m long tube filled with argon gas to generate a visible continuum. The two colortunable pulses indicated in Figure 1 are produced by filtering 5 nm wide portions of this continuum in a pair of all-reflective 4F setups with a motorized slits at the 2F planes. <sup>16</sup> These 115 pJ, 250 fs laser pulses are focused to the spots sizes of 82  $\mu$ m on the photovoltaic device, which is consistent with the fluences employed in other NLPC-like experiments. <sup>25,28,52</sup>

For NLPC spectroscopy, the photocurrent produced by the device is amplified at 500 nA/V using a Stanford Research 570 current preamplifier to maximize the dynamic range of the detection system. Signals are then processed with a National Instruments data acquisition board (NI USB-6221) that is synchronized to the laser system at 250 Hz (i.e., divide laser's repetition rate by 4). An adequate density of points is obtained by setting the sampling rate of the data acquisition board to 500 kHz. The two laser beams are chopped at 500 and 250 Hz to enable signal detection under four conditions: pulse 1 only  $(S_1)$ , pulse 2 only  $(S_2)$ , pulses 1 and 2  $(S_{1+2})$ , and both pulses blocked  $(S_0)$ . The NLPC signal, which is reported in units of nA in Figure 2, is defined as  $S_{NLPC} = S_{1+2} - S_1 - S_2 + S_0^{26,28}$ The signal is averaged over a total of 800 laser shots at each point. The delays and wavelengths, which are scanned in 5 nm steps, are cycled 5 times and averaged for a total data acquisition time of 6 h. The spectra in Figure 2 represent the average for three separate devices.

NLFL spectroscopy is conducted using the same experimental setup employed for NLPC experiments. Fluorescence emission from the films is collected using a 5 cm diameter, 5 cm focal length achromatic lens and relayed to 5 cm diameter, 7.5 cm focal length achromatic lens, which focuses the emission onto a photomultiplier tube (PMT, ThorLabs #PMM02). The signal is amplified by applying a 0.7 V control voltage to the PMT before processing with a National Instruments data acquisition board (NI USB-6221) that is synchronized to the laser system at 250 Hz with a sampling rate of 500 kHz. Contributions from scattered light are minimized using an iris and interference filter (Edmund Optics #86-955) that is centered at 725 nm with a 50 nm bandpass. The 50 nm wide bandpass yields sufficient signal-to-noise ratio, while still allowing the laser beams to be tuned from 500 to 690 nm. The two laser beams are chopped at 500 and 250 Hz, and the NLFL signal is defined as  $S_{\rm NLFL}$  =  $S_{1+2}$  -  $S_1$  -  $S_2$  +  $S_0$ . The signal is averaged over a total of 800 laser shots at each point. The delay times and wavelengths, which are scanned in 5 nm steps, are cycled 10 times and averaged for a total data acquisition time of 24 h.

## ASSOCIATED CONTENT

## Supporting Information

The Supporting Information is available free of charge at https://pubs.acs.org/doi/10.1021/acs.jpclett.0c00844.

NLPC and NLFL spectra acquired for multiple samples, discussion of the origins of cross peaks in transient absorption spectra, and fitting of the data in Figure 3 to sums of exponential functions (PDF)

## AUTHOR INFORMATION

## **Corresponding Author**

Andrew M. Moran — Department of Chemistry, University of North Carolina at Chapel Hill, Chapel Hill, North Carolina 27599, United States; ⊚ orcid.org/0000-0001-7761-7613; Email: ammoran@email.unc.edu

#### Authors

- Ninghao Zhou Department of Chemistry, University of North Carolina at Chapel Hill, Chapel Hill, North Carolina 27599, United States
- **Zhenyu Ouyang** Department of Chemistry, University of North Carolina at Chapel Hill, Chapel Hill, North Carolina 27599, United States
- Jun Hu − Department of Chemistry, University of North Carolina at Chapel Hill, Chapel Hill, North Carolina 27599, United States; Oorcid.org/0000-0002-6997-0174
- Olivia F. Williams Department of Chemistry, University of North Carolina at Chapel Hill, Chapel Hill, North Carolina 27599, United States
- Liang Yan Department of Chemistry, University of North Carolina at Chapel Hill, Chapel Hill, North Carolina 27599, United States; oorcid.org/0000-0003-4122-7466
- Wei You Department of Chemistry, University of North Carolina at Chapel Hill, Chapel Hill, North Carolina 27599, United States; ⊙ orcid.org/0000-0003-0354-1948

Complete contact information is available at: https://pubs.acs.org/10.1021/acs.jpclett.0c00844

## **Author Contributions**

<sup>†</sup>N.Z. and Z.O. contributed equally to this work.

### Notes

The authors declare no competing financial interest.

# ACKNOWLEDGMENTS

This work is supported by the National Science Foundation under CHE-1763207 (N.Z., Z.O., O.F.W., and A.M.M.). J.H., L.Y., and W.Y. acknowledge support from UNC Research Opportunities Initiative (ROI) through the Center of Hybrid Materials Enabled Electronic Technology. Research of 2D perovskites fabrication was supported by the Center for Hybrid Organic Inorganic Semiconductors for Energy (CHOISE), an Energy Frontier Research Center funded by the U.S. Department of Energy (DOE), Office of Science, Office of Basic Energy Sciences (BES).

# **■ REFERENCES**

- (1) Kojima, A.; Teshima, K.; Shirai, Y.; Miyasaka, T. Organometal Halide Perovskites as Visible-Light Sensitizers for Photovoltaic Cells. *J. Am. Chem. Soc.* **2009**, *131*, 6050–6051.
- (2) Lee, M. M.; Teuscher, J.; Miyasaka, T.; Murakami, T. N.; Snaith, H. J. Efficient Hybrid Solar Cells Based on Meso-Superstructured Organometal Halide Perovskites. *Science* **2012**, *338*, 643–647.
- (3) Kim, H. S.; Lee, C.-R.; Im, J.-H.; Lee, K.-B.; Moehl, T.; Marchioro, A.; Moon, S.-J.; Humphry-Baker, R.; Yum, J.-H.; Moser, J. E.; et al. Lead Iodide Perovskite Sensitized All-Solid-State Submicron Thin Film Mesoscopic Solar Cell with Efficiency Exceeding 9%. *Sci. Rep.* 2012, 2, 591.
- (4) Best Research-Cell Efficiencies. U.S. Department of Energy; National Renewal Energy Laboratory, 2019.
- (5) Burschka, J.; Pellet, N.; Moon, S.-J.; Humphry-Baker, R.; Gao, P.; Nazeeruddin, M. K.; Grätzel, M. Sequential Deposition as a Route to High-Performance Perovskite-Sensitized Solar Cells. *Nature* **2013**, 499, 316–319.

- (6) Fang, Y.; Dong, Q.; Shao, Y.; Yuan, Y.; Huang, J. Highly Narrowband Perovskite Single-Crystal Photodetectors Enabled by Surface-Charge Recombination. *Nat. Photonics* **2015**, *9*, 679–686.
- (7) Hao, F.; Stoumpos, C. C.; Cao, D. H.; Chang, R. P.; Kanatzidis, M. G. Lead-Free Solid-State Organic-Inorganic Halide Perovskite Solar Cells. *Nat. Photonics* **2014**, *8*, 489–494.
- (8) Niu, G.; Guo, X.; Wang, L. Review of Recent Progress in Chemical Stability of Perovskite Solar Cells. *J. Mater. Chem. A* **2015**, 3, 8970–8980.
- (9) Smith, I. C.; Hoke, E. T.; Solis-ibarra, D.; Mcgehee, M. D.; Karunadasa, H. I. A Layered Hybrid Perovskite Solar-Cell Absorber with Enhanced Moisture Stability. *Angew. Chem., Int. Ed.* **2014**, *53*, 11232–11235.
- (10) Xing, J.; Zhao, Y.; Askerka, M.; Quan, L. N.; Gong, X.; Zhao, W.; Zhao, J.; Tan, H.; Long, G.; Gao, L.; et al. Color-stable highly luminescent sky-blue perovskite light-emitting diodes. *Nat. Commun.* **2018**, *9*, 3541.
- (11) Zhang, J.; Qin, J.; Wang, M.; Bai, Y.; Zou, H.; Keum, J. K.; Tao, R.; Xu, H.; Yu, H.; Haacke, S.; Hu, B. Uniform Permutation of Quasi-2D Perovskites by Vacuum Poling for Efficient, High-Fill-Factor Solar Cells. *Joule* **2019**, *3*, 3061–3071.
- (12) Ren, H.; Yu, S.; Chao, L.; Xia, Y.; Sun, Y.; Zuo, S.; Li, F.; Niu, T.; Yang, Y.; Ju, H.; et al. Efficient and Stable Ruddlesden–Popper Perovskite Solar Cell with Tailored Interlayer Molecular Interaction. *Nat. Photonics* **2020**, *14*, 154–163.
- (13) Stoumpos, C. C.; Cao, D. H.; Clark, D. J.; Young, J.; Rondinelli, J. M.; Jang, J. I.; Hupp, J. T.; Kanatzidis, M. G. Ruddlesden—Popper Hybrid Lead Iodide Perovskite 2D Homologous Semiconductors. *Chem. Mater.* **2016**, *28*, 2852—2867.
- (14) Blancon, J.-C.; Tsai, H.; Nie, W.; Stoumpos, C. C.; Pedesseau, L.; Katan, C.; Kepenekian, M.; Soe, C. M. M.; Appavoo, K.; Sfeir, M. Y.; et al. Extremely Efficient Internal Exciton Dissociation Through Edge States in Layered 2D Perovskites. *Science* **2017**, 355, 1288–1292.
- (15) Liu, J.; Leng, J.; Wu, K.; Zhang, J.; Jin, S. Observation of Internal Photoinduced Electron and Hole Separation in Hybrid Two-Dimensional Perovskite Films. *J. Am. Chem. Soc.* **2017**, *139*, 1432–1435
- (16) Williams, O. F.; Guo, Z.; Hu, J.; Yan, L.; You, W.; Moran, A. M. Energy Transfer Mechanisms in Layered 2D Perovskites. *J. Chem. Phys.* **2018**, *148*, 134706.
- (17) Yan, L.; Hu, J.; Guo, Z.; Chen, H.; Toney, M. F.; Moran, A. M.; You, W. General Post-Annealing Method Enables High-Efficiency Two-Dimensional Perovskite Solar Cells. *ACS Appl. Mater. Interfaces* **2018**, *10*, 33187–33197.
- (18) Williams, O. F.; Zhou, N.; Hu, J.; Ouyang, Z.; Kumbhar, A.; You, W.; Moran, A. M. Imaging Excited State Dynamics in Layered 2D Perovskites with Transient Absorption Microscopy. *J. Phys. Chem.* A 2019, 123, 11012–11021.
- (19) Cao, D. H.; Stoumpos, C. C.; Farha, O. K.; Hupp, J. T.; Kanatzidis, M. G. 2D Homologous Perovskites as Light-Absorbing Materials for Solar Cell Applications. *J. Am. Chem. Soc.* **2015**, *137*, 7843–7850.
- (20) Ogomi, Y.; Morita, A.; Tsukamoto, S.; Saitho, T.; Fujikawa, N.; Shen, Q.; Toyoda, T.; Yoshino, K.; Pandey, S. S.; Ma, T.; et al.  $CH_3NH_3Sn_xPb_{(1-x)}I_3$  perovskite solar cells covering up to 1060 nm. *J. Phys. Chem. Lett.* **2014**, *5*, 1004–1011.
- (21) Silver, S.; Yin, J.; Li, H.; Brédas, J. L.; Kahn, A. Characterization of the valence and conduction band levels of n=1 2D perovskites: A combined experimental and theoretical investigation. *Adv. Energy Mater.* **2018**, *8*, 1703468.
- (22) Shang, Q.; Wang, Y.; Zhong, Y.; Mi, Y.; Qin, L.; Zhao, Y.; Qiu, X.; Liu, X.; Zhang, Q. Unveiling Structurally Engineered Carrier Dynamics in Hybrid Quasi-Two-Dimensional Perovskite Thin Films Toward Controllable Emission. *J. Phys. Chem. Lett.* **2017**, *8*, 4431–4438
- (23) Zhang, L.; Zhang, X.; Lu, G. Band Alignment in Two-Dimensional Halide Perovskite Heterostructures: Type I or Type II? *J. Phys. Chem. Lett.* **2020**, *11*, 2910–2916.

- (24) Tekavec, P. F.; Lott, G. A.; Marcus, A. H. Fluorescence-Detected Two-Dimensional Electronic Coherence Spectroscopy by Acousto-Optic Phase Modulation. *J. Chem. Phys.* **2007**, *127*, 214307.
- (25) Nardin, G.; Autry, T. M.; Silverman, K. L.; Cundiff, S. T. Multidimensional Coherent Photocurrent Spectroscopy of a Semi-conductor Nanostructure. *Opt. Express* **2013**, *21*, 28617–28627.
- (26) Karki, K. J.; Widom, J. R.; Seibt, J.; Moody, I.; Lonergan, M. C.; Pullerits, T.; Marcus, A. H. Coherent Two-Dimensional Photocurrent Spectroscopy in a PbS Quantum Dot Photocell. *Nat. Commun.* **2014**, *5*, 5869.
- (27) Vella, E.; Li, H.; Grégoire, P.; Tuladhar, S. M.; Vezie, M. S.; Few, S.; Bazán, C. M.; Nelson, J.; Silva-Acuña, C.; Bittner, E. R. Ultrafast Decoherence Dynamics Govern Photocarrier Generation Efficiencies in Polymer Solar Cells. *Sci. Rep.* **2016**, *6*, 29437.
- (28) Zhou, N.; Hu, J.; Ouyang, Z.; Williams, O. F.; Yan, L.; You, W.; Moran, A. M. Nonlinear Photocurrent Spectroscopy of Layered 2D Perovskite Quantum Wells. J. Phys. Chem. Lett. 2019, 10, 7362–7367.
- (29) Malý, P.; Mančal, T. Signatures of Exciton Delocalization and Exciton—Exciton Annihilation in Fluorescence-Detected Two-Dimensional Coherent Spectroscopy. *J. Phys. Chem. Lett.* **2018**, *9*, 5654—5659
- (30) Tiwari, V.; Matutes, Y. A.; Gardiner, A. T.; Jansen, T. L. C.; Cogdell, R. J.; Ogilvie, J. P. Spatially-Resolved Fluorescence-Detected Two-Dimensional Electronic Spectroscopy Probes Varying Excitonic Structure in Photosynthetic Bacteria. *Nat. Commun.* **2018**, *9*, 4219.
- (31) Karki, K. J.; Chen, J.; Sakurai, A.; Shi, Q.; Gardiner, A. T.; Kühn, O.; Cogdell, R. J.; Pullerits, T. Before Förster. Initial excitation in photosynthetic light harvesting. *Chem. Sci.* **2019**, *10*, 7923–7928.
- (32) Hu, J.; Oswald, I. W. H.; Stuard, S. J.; Nahid, M. M.; Zhou, N.; Williams, O. F.; Guo, Z.; Yan, L.; Hu, H.; Chen, Z.; et al. Synthetic Control over Orientational Degeneracy of Spacer Cations Enhances Solar Cell Efficiency in Two-Dimensional Perovskites. *Nat. Commun.* **2019**, *10*, 1276.
- (33) Wu, X.; Trinh, M. T.; Zhu, X.-Y. Excitonic Many-Body Interactions in Two-Dimensional Lead Iodide Perovskite Quantum Wells. *J. Phys. Chem. C* **2015**, *119*, 14714–14721.
- (34) Damtie, F. A.; Wacker, A.; Pullerits, T.; Karki, K. J. Two-Dimensional Action Spectroscopy of Excitonic Systems: Explicit Simulation Using a Phase-Modulation Technique. *Phys. Rev. A: At., Mol., Opt. Phys.* **2017**, *96*, No. 053830.
- (35) Hong, X.; Ishihara, T.; Nurmikko, A. V. Dielectric Confinement Effect on Excitons in PbI<sub>4</sub>-Based Layered Semiconductors. *Phys. Rev. B: Condens. Matter Mater. Phys.* **1992**, *45*, 6961–6964.
- (36) Muljarov, E. A.; Tikhodeev, S. G.; Gippius, N. A.; Ishihara, T. Excitons in Self-Organized Semiconductor/Insulator Superlattices: PbI-Based Perovskite Compounds. *Phys. Rev. B: Condens. Matter Mater. Phys.* 1995, 51, 14370–14377.
- (37) Nitzan, A. Chemical Dynamics in Condensed Phases; Oxford University Press: Oxford, 2006.
- (38) Tomita, A.; Shah, J.; Knox, R. S. Efficient Exciton Energy Transfer Between Widely Separated Quantum Wells at Low Temperatures. *Phys. Rev. B: Condens. Matter Mater. Phys.* **1996**, 53, 10793–10803.
- (39) Proppe, A. H.; Elkins, M. H.; Voznyy, O.; Pensack, R. D.; Zapata, F.; Besteiro, L. V.; Quan, L. N.; Quintero-Bermudez, R.; Todorovic, P.; Kelley, S. O.; et al. Spectrally Resolved Ultrafast Exciton Transfer in Mixed Perovskite Quantum Wells. J. Phys. Chem. Lett. 2019, 10, 419–426.
- (40) Krueger, B. P.; Scholes, G. D.; Fleming, G. R. Calculation of Couplings and Energy-Transfer Pathways between the Pigments of LH2 by the ab Initio Transition Density Cube Method. *J. Phys. Chem. B* **1998**, *102*, 5378–5386.
- (41) Abramavicius, D.; Mukamel, S. Many-Body Approaches for Simulating Coherent Nonlinear Spectroscopies of Electronic and Vibrational Excitons. *Chem. Rev.* **2004**, *104*, 2073–2098.
- (42) Schlau-Cohen, G. S.; Ishizaki, A.; Fleming, G. R. Two-dimensional Electronic Spectroscopy and Photosynthesis: Fundamentals and Applications to Photosynthetic Light-Harvesting. *Chem. Phys.* **2011**, 386, 1–22.

- (43) Kitazawa, N.; Watanabe, Y.; Nakamura, Y. Optical properties of CH<sub>3</sub>NH<sub>3</sub>PbX<sub>3</sub> (X = halogen) and their mixed-halide crystals. *J. Mater. Sci.* **2002**, *37*, 3585–3587.
- (44) Noh, J. H.; Im, S. H.; Heo, J. H.; Mandal, T. N.; Seok, S. I. Chemical management for colorful, efficient, and stable inorganic-organic hybrid nanostructured solar cells. *Nano Lett.* **2013**, *13*, 1764–1769
- (45) Kulkarni, S. A.; Baikie, T.; Boix, P. P.; Yantara, N.; Mathews, N.; Mhaisalkar, S. Band-gap tuning of lead halide perovskites using a sequential deposition process. *J. Mater. Chem. A* **2014**, *2*, 9221–9225.
- (46) McMeekin, D. P.; Sadoughi, G.; Rehman, W.; Eperon, G. E.; Saliba, M.; Horantner, M. T.; Haghighirad, A.; Sakai, N.; Korte, L.; Rech, B.; et al. A mixed-cation lead mixed-halide perovskite absorber for tandem solar cells. *Science* **2016**, *351*, 151–155.
- (47) Bai, Y.; Xiao, S.; Hu, C.; Zhang, T.; Meng, X.; Lin, H.; Yang, Y.; Yang, S. Dimensional Engineering of a Graded 3D-2D Halide Perovskite Interface Enables Ultrahigh  $V_{\rm oc}$  Enhanced Stability in the p-i-n Photovoltaics. *Adv. Energy Mater.* **2017**, *7*, 1701038.
- (48) Wang, Z.; Lin, Q.; Chmiel, F. P.; Sakai, N.; Herz, L. M.; Snaith, H. J. Efficient ambient-air-stable solar cells with 2D–3D heterostructured butylammonium-caesium-formamidinium lead halide perovskites. *Nat. Energy* **2017**, *2*, 17135.
- (49) Li, M. H.; Yeh, H. H.; Chiang, Y. H.; Jeng, U. S.; Su, C. J.; Shiu, H. W.; Hsu, Y. J.; Kosugi, N.; Ohigashi, T.; Chen, Y. A.; et al. Highly Efficient 2D/3D Hybrid Perovskite Solar Cells via Low-Pressure Vapor-Assisted Solution Process. *Adv. Mater.* **2018**, *30*, No. 1801401.
- (50) Zou, Y.; Cui, Y.; Wang, H. Y.; Cai, Q.; Mu, C.; Zhang, J. P. Highly efficient and stable 2D-3D perovskite solar cells fabricated by interfacial modification. *Nanotechnology* **2019**, *30*, 275202.
- (51) Zhou, Y.; Wang, F.; Cao, Y.; Wang, J.-P.; Fang, H.-H.; Loi, M. A.; Zhao, N.; Wong, C.-P. Benzylamine-Treated Wide-Bandgap Perovskite with High Thermal-Photostability and Photovoltaic Performance. *Adv. Energy Mater.* **2017**, *7*, 1701048.
- (52) Grégoire, P.; Kandada, A. R. S.; Vella, E.; Tao, C.; Leonelli, R.; Silva, C. Incoherent Population Mixing Contributions to Phase-Modulation Two-Dimensional Coherent Excitation Spectra. *J. Chem. Phys.* **2017**, *147*, 114201.